ADVANCED FUNCTIONAL MATERIALS
www.afm-journal.de

A General Strategy for Enhancing Sensitivity and Suppressing Noise in Infrared Organic Photodetectors Using Non-Conjugated Polymer Additives

*Tyler Bills, Chih-Ting Liu, Jasmine Lim, Naresh Eedugurala, Paramasivam Mahalingavelar, Bogyeom Seo, Ethan T. Hanna, Tse Nga Ng, and Jason D. Azoulay**

Photodetectors operating across the near- to short-wave infrared (NIR–SWIR, λ = 0.9–1.8 µm) underpin modern science, technology, and society. Organic photodiodes (OPDs) based on bulk-heterojunction (BHJ) active layers overcome critical manufacturing and operating drawbacks inherent to crystalline inorganic semiconductors, offering the potential for low-cost, uncooled, mechanically compliant, and ubiquitous infrared technologies. A constraining feature of these narrow bandgap materials systems is the high noise current under an applied bias, resulting in specific detectivities (D^*, the figure of merit for detector sensitivity) that are too low for practical utilization. Here, this study demonstrates that incorporating wide-bandgap insulating polymers within the BHJ suppresses noise by diluting the transport and trapping sites as determined using capacitance-frequency analysis. The resulting D^* of NIR–SWIR OPDs operating from 600–1400 nm under an applied bias of −2 V is improved by two orders of magnitude, from 10^8 to 10^{10} Jones (cm $Hz^{1/2}$ W^{-1}), when incorporating polysulfone within the blends. This broadly applicable strategy can reduce noise in IR-OPDs enabling their practical operation and the realization of emerging technologies.

1. Introduction

Emerging technologies with global societal impacts in renewable energy, healthcare, information science, building and machine automation, and consumer applications require ubiquitous, uncooled, low-cost, and mechanically compliant photodetection technologies operating across the near- to short-wave infrared (NIR–SWIR, λ = 0.9–1.8 µm).[1–7] Despite widespread efforts in scientific and engineering disciplines, photodetectors operating beyond the cut-off of silicon ($\lambda_c \approx 1.1$ µm) remain dependent on archetypal crystalline inorganic semiconductors such as germanium (Ge, λ = 0.4–2.0 µm), alloys of indium gallium arsenide (InGaAs, λ = 0.4–2.4 µm), and materials such as lead sulfide (PbS, λ = 1–3 µm) and lead selenide (PbSe, λ = 1–5 µm).[8] Devices fabricated using these materials require high-costs, complex manufacturing processes (e.g., multistep processes of physical or chemical evaporation, photolithography, complex die transfer, and bonding), cooling, are largely incompatible with silicon-based technologies, and require the use of toxic materials (As, Pb) and critical (Ga, Ge) elements. These attributes are prohibitive for their widespread utilization and the development of emerging technologies.

Organic photodiodes (OPDs) comprised of organic semiconductors (OSCs) overcome critical manufacturing and operating drawbacks inherent to these inorganic semiconductors. The active layer of these devices is comprised of a bulk heterojunction (BHJ) architecture, with intermixed *p*-type (donor) and *n*-type (acceptor) OSCs. BHJ active layers provide significant

T. Bills, C.-T. Liu, N. Eedugurala, P. Mahalingavelar, J. D. Azoulay
School of Chemistry and Biochemistry and School of Materials Science and Engineering
Georgia Institute of Technology
Atlanta, GA 30332, USA
E-mail: jdazoulay@gatech.edu

J. Lim, E. T. Hanna
School of Polymer Science and Engineering
The University of Southern Mississippi
Hattiesburg, MS 39406, USA

B. Seo, T. N. Ng
Department of Electrical and Computer Engineering
University of California San Diego
La Jolla, CA 92161, USA

The ORCID identification number(s) for the author(s) of this article can be found under https://doi.org/10.1002/adfm.202314210

DOI: 10.1002/adfm.202314210

advantages including ease of synthesis, very high absorption coefficients, monolithic integration with silicon electronics, uncooled operation, and the potential for low-cost, large-area, and scalable fabrication.[2–7,9,10] Moreover, OSCs are comprised of non-toxic and earth abundant materials (e.g., C, H, N, S), are tolerant toward structural defects and disorder, and offer the capability to be fabricated into diverse and mechanically compliant form factors. These attributes offer opportunities for emerging technologies that are unavailable from other semiconductor materials.[3–7,9,10] Despite these advantages, state-of-the-art OPDs primarily operate in the visible region of the electromagnetic spectrum. However, progress in materials design and synthesis have led to the development of a new generation of OSCs with narrower bandgaps that enable optical to electrical transduction of longer-wavelength NIR–SWIR light.[11–14]

A figure of merit that compares the sensitivity and performance between different detector technologies is the specific detectivity (D^*). Values for D^* of 10^{12} Jones (cm $Hz^{1/2}$ W^{-1}) or higher have been routinely reported for OPDs operating in the visible.[15,16] In contrast, D^* is typically several orders of magnitude lower for NIR–SWIR OPDs.[10,17–19] While D^* ranging from $\approx 10^{11}$–10^{12} Jones has been reported within a spectral range of 0.6–1.4 µm,[4,20–24] these measurements do not always account for all contributions to the noise, a key factor that dictates the performance and sensitivity of a photodetector. Furthermore, OPDs usually operate in reverse bias, where the measured reverse dark current (J_{dark}) rises significantly from the value at 0 V. Thus, biasing increases the noise current density, resulting in D^* under practical operating conditions that is too low for practical application, thereby limiting the utilization of these emerging semiconductor materials. This fundamental limitation means that inorganic semiconductor devices remain the only viable technology for sensitively detecting faint NIR–SWIR electromagnetic radiation.[8,25]

In this study, we provide a versatile strategy to reduce noise under an applied bias, which relies on incorporating wide bandgap polymers within the BHJ. The addition of non-conjugated and insulating polymers to OSC active layers has precedence in organic photovoltaics (OPVs) and organic field-effect transistors (OFETs).[26–28] These studies have demonstrated a retention of critical optical and electronic properties of the active material while improving overall device performance metrics. However, there have been few reports that investigate the incorporation of these materials within OPDs.[29,30] Here, we demonstrate that incorporating wide-bandgap insulating polymers within the BHJ suppresses noise by diluting the transport and trapping sites. The resulting D^* of NIR–SWIR OPDs operating from 600–1400 nm under an applied bias of −2 V is improved by two orders of magnitude, from 10^8 to 10^{10} Jones (cm $Hz^{1/2}$ W^{-1}), when incorporating polysulfone within the blends. With the preservation of charge-transfer interfaces and a percolating conductive network, the decrease in noise, due to trap dilution, outpaces the reduction in light harvesting efficiency. Thus, this broadly applicable strategy can reduce noise in IR-OPDs enabling their practical operation and the realization of emerging technologies.

2. Results and Discussion

To establish a performance baseline, we utilized a model system comprised of the IR sensitive donor-acceptor conjugated polymer poly(4-(5-(4-(3,5-bis(dodecyloxy)benzylidene)-4*H*-cyclopenta[2,1-*b*:3,4-*b*']dithiophen-2-yl)thiophen-2-yl)-6,7- dioctyl-9-(thiophen-2-yl) [1,2,5]thiadiazolo[3,4-*g*]quinoxaline)[18] (CDT-TQ) in combination with a fullerene acceptor [6,6]-phenyl-C_{71}-buytic acid methyl ester ($PC_{71}BM$) as the photoactive layer (**Figure 1a**). We fabricated OPD devices with an indium tin oxide [ITO]/poly(3,4-ethylenedioxythiophene):poly(styrenesulfonate)[PEDOT:PSS]/CDT-TQ:$PC_{71}BM$/ZnO/Al architecture (Figure 1b). Insulating polymers including polystyrene (PS), poly(methyl methacrylate) (PMMA), and polysulfone (PSU) were blended into the active layers of these devices at varying concentrations (Figure 1c,d). Full details regarding the synthesis of the polymer and device fabrication can be found in the Supporting Information.

We first examined the properties of a control OPD comprised of a binary blend of CDT-TQ and $PC_{71}BM$ in a 1:2 ratio. Current density–voltage (*J*–*V*) measurements of the control device at 0 V yields an external quantum efficiency (EQE) of 25% at 1100 nm with a measurable response to 1400 nm (**Figure 2a,b**). This gives a responsivity (R) of 0.20 A W^{-1} at 1100 nm, among the highest value reported for polymer-based OPDs. The specific detectivity (D^*) given in units of Jones (cm $Hz^{1/2}$ W^{-1}) enables a performance comparison between different detector technologies with a singular figure of merit, and is the signal-to-noise ratio given by:

$$D^* = \frac{q\lambda\sqrt{A}}{hc}\ \frac{EQE}{i_n} = \frac{R\sqrt{A}}{i_n} \tag{1}$$

where q is the elementary charge, λ the wavelength, h the Planck constant, c the speed of light, A the device area in cm^2, R the responsivity in A W^{-1}, and i_n is the noise current spectral density (total noise of a photodiode) in A $Hz^{-1/2}$. Applying a reverse bias of −2 V results in a concomitant increase in the EQE to 40% and an increase in R from 0.20 to 0.37 A W^{-1} (Figure 2b). However, this is accompanied by a reduction in D^* from 2.1×10^{11} Jones at 0 V to 5.3×10^8 Jones at −2 V (Figure 2c). The total noise current was directly measured with a power spectrum analyzer to capture all the contributions to the noise and is given by:

$$i_n = \left({i_{1/f}}^2 + {i_{shot}}^2 + {i_{thermal}}^2\right)^{1/2} \tag{2}$$

where i_{shot} is the shot noise, $i_{thermal}$ is the thermal noise, and $i_{1/f}$ is the flicker noise. The application of a reverse bias results in an increase in the total noise (i_n) at 400 Hz from 1.9×10^{-13} A $Hz^{-1/2}$ at 0 V up to 1.4×10^{-10} A $Hz^{-1/2}$ at −2 V (Figure 2d), thereby reducing the overall D^*.

These results demonstrate that achieving a high signal-to-noise ratio in the NIR–SWIR is often challenging due to the inherently large dark currents in narrow bandgap materials systems. In BHJs comprised of semicrystalline conjugated polymers, fullerenes, and other molecular acceptors, sub-bandgap trap states affect charge transport and carrier recombination,

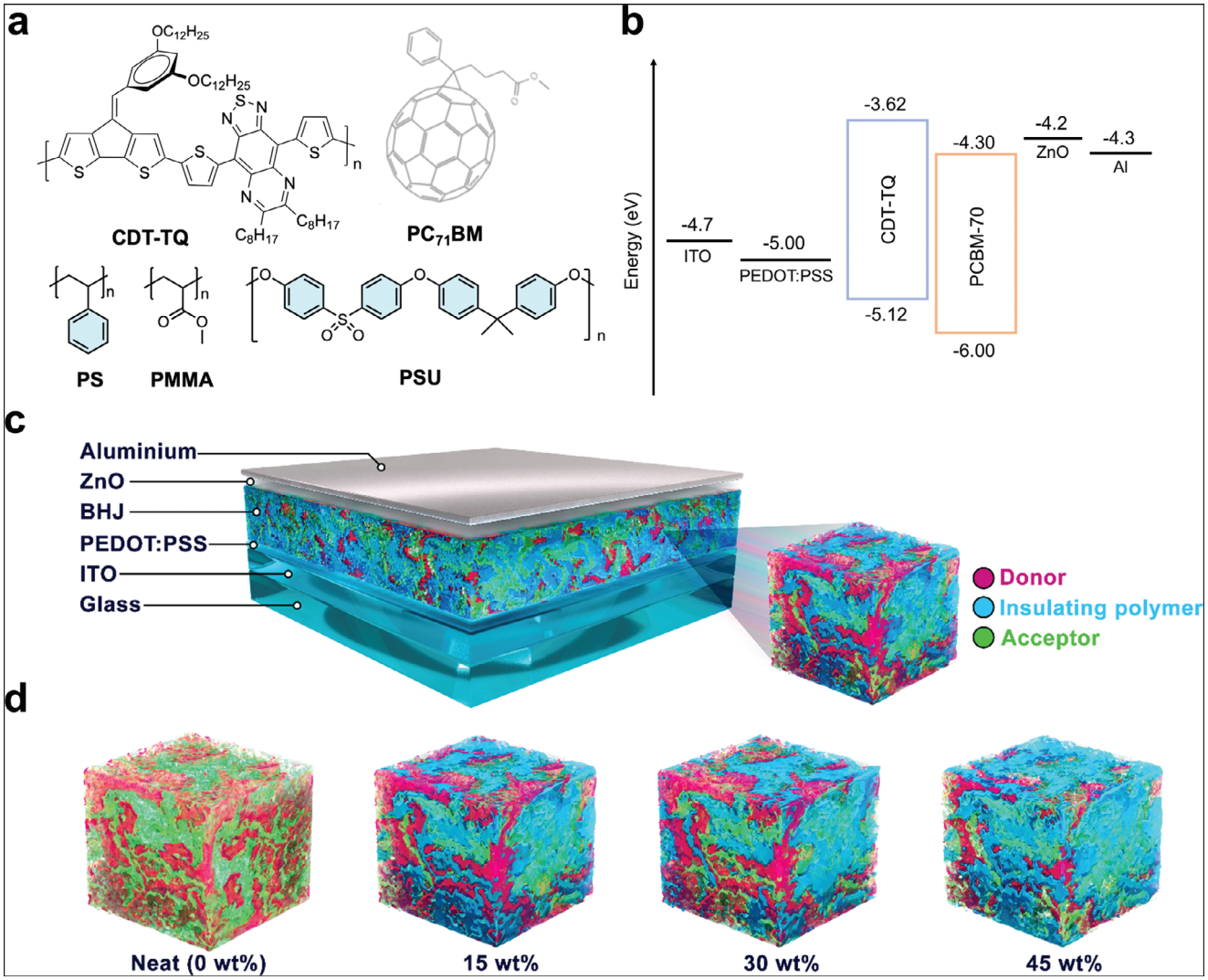

Figure 1. a) Chemical structures of the infrared active donor polymer (CDT-TQ), fullerene acceptor ($PC_{71}BM$), and PS, PMMA, and PSU. b) Energy level diagram of the ITO/PEDOT:PSS/CDT-TQ:$PC_{71}BM$/ZnO/Al photodiode. c,d) Depiction of the OPD structure and BHJ morphology upon increasing the content of insulating polymer.

thereby increasing i_n.[31–33] Unlike reverse bias conditions, common to OPD operation, the low level of dark current in the absence of a bias can be substantially affected by the presence of carrier trapping within these sub-bandgap states. However, previous studies have demonstrated that carrier trapping can be suppressed by diluting the transport and trapping sites of OSCs by blending with a wide-bandgap material or insulating polymer.[34,35] This motivated our investigation into whether this approach could be used to suppress the strong charge trapping and resulting high J_{dark} under bias in organic NIR–SWIR OPDs.

To address and understand these issues, we studied ternary systems comprised of our CDT-TQ:$PC_{71}BM$ combination blended with insulating polymers including polystyrene (PS), poly(methyl methacrylate) (PMMA), and polysulfone (PSU). PS and PMMA were chosen based on their ability to improve device performance by diluting the trap states encountered by charges and through tuning the existing OSC morphology.[26–28,36,37] Narrow bandgap conjugated polymers such as CDT-TQ are inherently more rigid that traditional semiconducting polymers, a structural feature that enables extended π-conjugation and interactions with longer wavelength light. It is well-established that rigid-rod and coiled macromolecules (PS and PMMA in this case) are highly immiscible[38]; thus, we also evaluated PSU, a rigid-rod aromatic thermoplastic.

For consistency, ternary blend devices were fabricated with the same architecture using CDT-TQ:$PC_{71}BM$ blends in a 1:2 ratio as utilized in the control devices (Figure 1). The active layers incorporated insulators at 15, 30, and 45 wt%. Briefly, blend solutions were prepared by diluting the insulating polymer in chlorobenzene, then dissolving CDT-TQ and $PC_{71}BM$ using this solution instead of neat solvent (see Supporting Information for full details). **Figure 3a** shows the dark current density–voltage (J–V) characteristics of the control OPD and those fabricated using different insulating polymers prepared using the 15% and 45 wt% solutions, with 30 wt% compared in Figure S2 (Supporting Information). The dark J–V curves demonstrate that as the

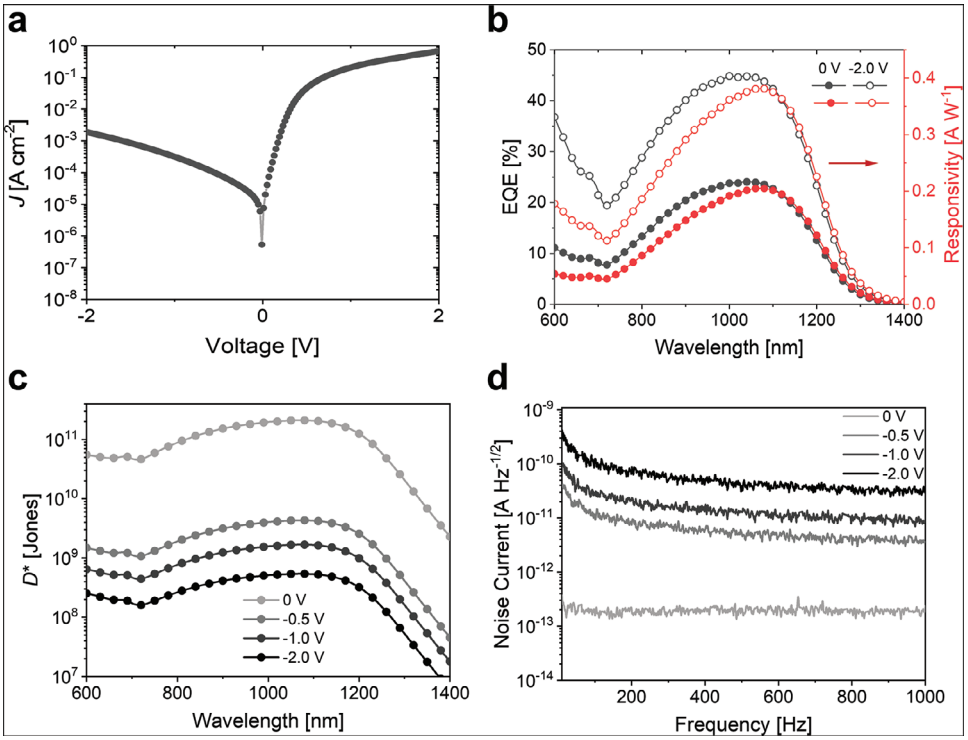

Figure 2. Photoresponse of the control OPD comprised of a 1:2 CDT-TQ:$PC_{71}BM$ blend. a) Current–voltage dark current density (*J–V*) curve. b) Responsivity and external quantum efficiency (EQE) of the device at 0 V and under an applied bias of −2 V. c) Specific detectivity (D^*) and d) noise spectral density from 0 to −2 V.

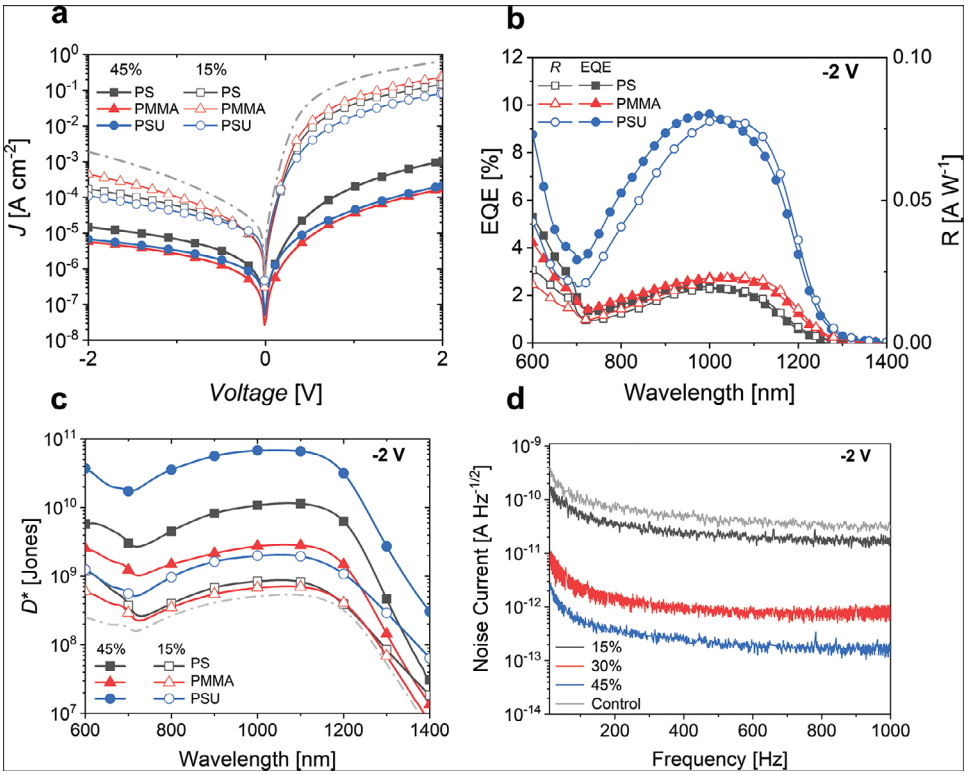

Figure 3. a) *J–V* curves of the OPDs in the dark with PS, PMMA, and PSU at 15 and 45 wt%. The control device is indicated by the dashed line. b) EQE and R under an applied bias of −2 V. c) Specific detectivity (D^*) of the 15 and 45 wt% OPDs at −2 V. d) Noise spectral density of PSU devices at 15, 30, and 45 wt% at −2 V.

Table 1. Comparison of the performance of CDT-TQ:$PC_{71}BM$ OPD and ternary blend OPDs incorporating PS, PMMA, and PSU at 15, 30, and 45 wt% under an applied bias of −2 V.

	i_n at 400 Hz [A $Hz^{-1/2}$]	$J_{-2\,V}$ [A cm^{-2}]	R at 1100 nm [A W^{-1}]	D^* at 1100 nm [Jones]
Control	1.4×10^{-10}	1.9×10^{-3}	0.37	5.3×10^{8}
PS_{15}	1.8×10^{-11}	2.9×10^{-5}	0.07	8.3×10^{8}
PS_{30}	8.1×10^{-13}	2.7×10^{-5}	0.03	7.1×10^{9}
PS_{45}	6.9×10^{-13}	2.4×10^{-6}	0.02	4.7×10^{9}
$PMMA_{15}$	2.7×10^{-11}	4.5×10^{-4}	0.09	7.0×10^{8}
$PMMA_{30}$	6.5×10^{-12}	1.1×10^{-4}	0.04	1.2×10^{9}
$PMMA_{45}$	1.6×10^{-12}	5.7×10^{-6}	0.02	2.9×10^{9}
PSU_{15}	2.2×10^{-11}	1.1×10^{-4}	0.21	1.9×10^{9}
PSU_{30}	9.1×10^{-13}	7.8×10^{-5}	0.11	2.4×10^{10}
PSU_{45}	2.3×10^{-13}	6.8×10^{-6}	0.07	6.6×10^{10}

concentration of insulating polymer increases, J_{dark} decreases by approximately three orders of magnitude compared to the control (1.9×10^{-3} at −2 V bias). Using concentrations of 45 wt%, J_{dark} at −2 V is 1.5×10^{-5}, 5.7×10^{-6}, and 6.8×10^{-6} A cm^{-2} for PS, PMMA, and PSU, respectively. This result is also accompanied by a decrease in EQE and R, as shown in Figure 3b. Increasing the insulator concentration up to 45 wt% decreases the peak EQE from 45% to ≈10% at 1100 nm under an applied bias of −2 V for PSU (Figure 3b) and to values as low as 2% for PS and PMMA. This demonstrates that diluting the active components with an insulating polymer also reduces the volumetric light harvesting efficiency of the blends, consistent with UV–vis–NIR absorption measurements comparing the control BHJ with the ternary blends (Figure S3, Supporting Information). These results starkly contrast those achieved in OPVs, where the addition of insulators increased EQE.[26–28,36,37] However, more optimal materials combinations may provide a similar enhancement. **Table 1** summarizes the performance parameters of ternary CDT-TQ:$PC_{71}BM$ OPDs incorporating PS, PMMA, and PSU at 15, 30, and 45 wt%. Examination of D^* at −2 V for the control device ($D^* = 5.3 \times 10^8$ Jones) and devices using 45 wt% solutions demonstrate a marked improvement using PS and PMMA ($D^* = 4.7 \times 10^9$ and 2.8×10^9 Jones, respectively), while the PSU device shows the highest $D^* = 6.6 \times 10^{10}$ Jones (Figure 3c).

The highest D^* at −2 V bias was obtained using PSU, prompting our detailed investigation of this ternary blend. We observed a decrease in $J_{-2\,V}$ from 1.1×10^{-4} to 6.8×10^{-6} A cm^{-2} as the PSU concentration was increased from 15 to 45 wt%, respectively (Figure 3a). While diluting the BHJ with insulator decreases the EQE, the total noise current under reverse bias also decreases from 1.4×10^{-10} A $Hz^{-1/2}$ for the control device to 2.3×10^{-13} A $Hz^{-1/2}$ at −2 V (Figure 3d). This decrease of over three orders of magnitude is consistent with a major suppression of the dominant contribution to the noise in devices incorporating PSU, resulting in a preservation of D^* upon applying a reverse bias (**Figure 4a**).

The addition of an inert component to the BHJs requires that the donor and acceptor semiconductors are sufficiently mixed to enable efficient exciton dissociation and charge separation. Each functional species must also form a percolating structure to allow efficient charge transport for electrons and holes to their respective electrodes. Atomic force microscopy (AFM) images of BHJ films incorporating PSU demonstrate that the insulator is mixed throughout the bulk of the composite films, increasingly diluting the active semiconductor components from 15 to 45 wt% (**Figure 5**). Without PSU, the BHJ film exhibits a smooth surface with a root-mean-square (RMS) roughness of 1.95 nm. Increasing the concentration of PSU to 15% increased the RMS roughness to 6.90 nm, while a further increase to 45% PSU decreased RMS roughness to 1.90 nm (Figure S4, Supporting Information). Additionally, the gradual addition of PSU increased the thickness of the active layer from 180 nm for the control device to 185, 226, and 460 nm at 15, 30, and 45 wt%, respectively. The large increase in thickness for PSU is likely a result of higher solution viscosity, which increases the thickness of spin coated films. Since differences in thickness may contribute to the noise suppression at the same potential, we have also normalized the dark current to the electric field (Figure S5, Supporting Information). The 45% PSU film still exhibits a dark photocurrent two orders of magnitude below that of the control, suggesting that the increased distance between the electrodes is not the deciding factor in noise reduction.

AFM-infrared spectroscopy (AFM-IR) was carried out to better understand the distribution of components within the blends. In the absence of PSU, a prototypical BHJ morphology is evident. At 15 wt% PSU, larger domains are present that contain

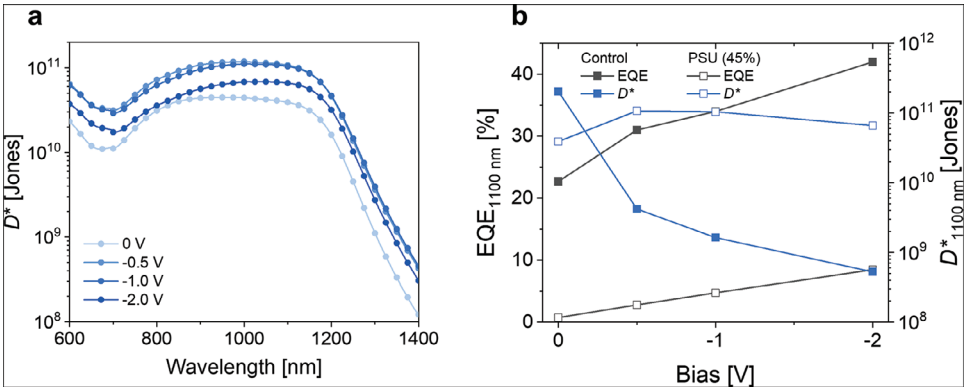

Figure 4. a) Specific detectivity of the 45 wt% PSU device at various applied biases. b) Bias-dependent EQE and specific detectivity at 1100 nm compared with the control device.

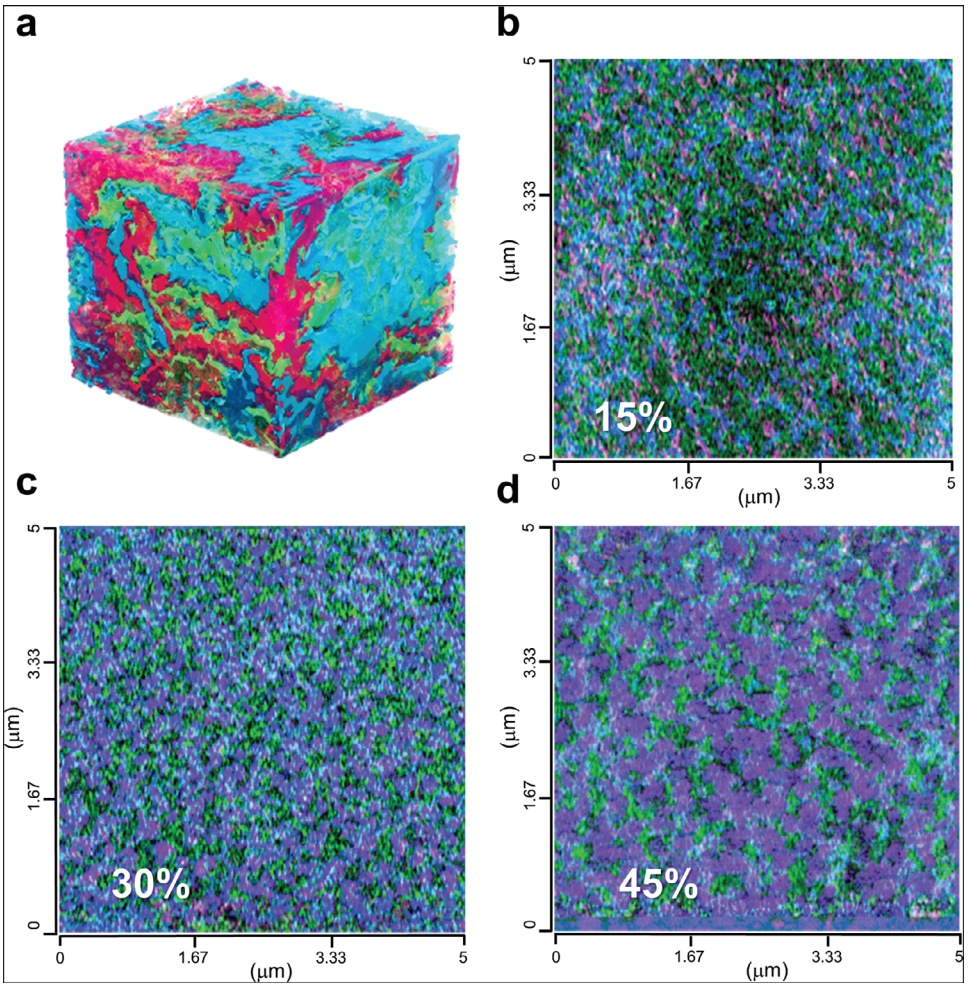

Figure 5. a) Pictorial representation of the spatial distribution of components in the active layer of a BHJ with PSU. b–d) AFM-IR topography images of the CDT-TQ:$PC_{71}BM$:PSU ternary blends with PSU incorporated at 15, 30, and 45 wt%, respectively. Color-coded as CDT-TQ (pink), $PC_{71}BM$ (green), and PSU (blue).

semiconductors and insulators (Figure 5b). The progressive addition of PSU at 30 and 45 wt% results in more pronounced intermixing of CDT-TQ, $PC_{71}BM$, and PSU (Figure 5c,d; Figures S6–S10, Supporting Information). The charge carrier mobilities of the control and ternary blend PSU device (45 wt%) were characterized by measuring the space charge-limited (SCLC) current of the active layers to investigate the effect of PSU addition (Figure S11, Supporting Information). The carrier mobility (μ) under an applied bias of 1.5 V was extracted from the J–V curves using Equation (3) where ϵ is the dielectric constant and L is the active layer thickness.

$$J_{SCLC} = \frac{9}{8}\,\epsilon\mu\frac{V^2}{L^3} \tag{3}$$

The mobility was estimated at 8.5×10^{-4} cm^2 V^{-1} s^{-1} at 0 wt% and was reduced to 1.1×10^{-5} cm^2 V^{-1} s^{-1} at 45 wt%, consistent with the increase of the domain sizes and film thickness with high PSU content. These results suggest that ideal insulative additives must balance bulk incorporation, morphological evolution, and signal to noise tradeoff.

Trap states (i.e., defect states) with intra-gap energies are prevalent within BHJ OPDs on account of the disordered nature of OSCs, structural defects, varying morphological features, the presence of impurities, and other contributions.[39] Depending on their energetic distance from the valence band, these traps can act as recombination centers, capture charge carriers, or contribute to the thermal dark current. To further understand how the trap density of the BHJs evolved with the addition of PSU, we utilized capacitance–frequency (C–ω) measurements to estimate the density-of-states (DOS) distribution. Capacitance-frequency or admittance spectroscopy has long been used to estimate the energetic distribution of trap states in semiconductor materials.[40–42] In these measurements, an applied AC bias modulates the occupation of trap states near the Fermi energy, enabling a determination of the fraction of trapped charges that are thermally excited to mobile transport states. The trap energy (E_ω), corresponds to traps within the bandgap that can respond

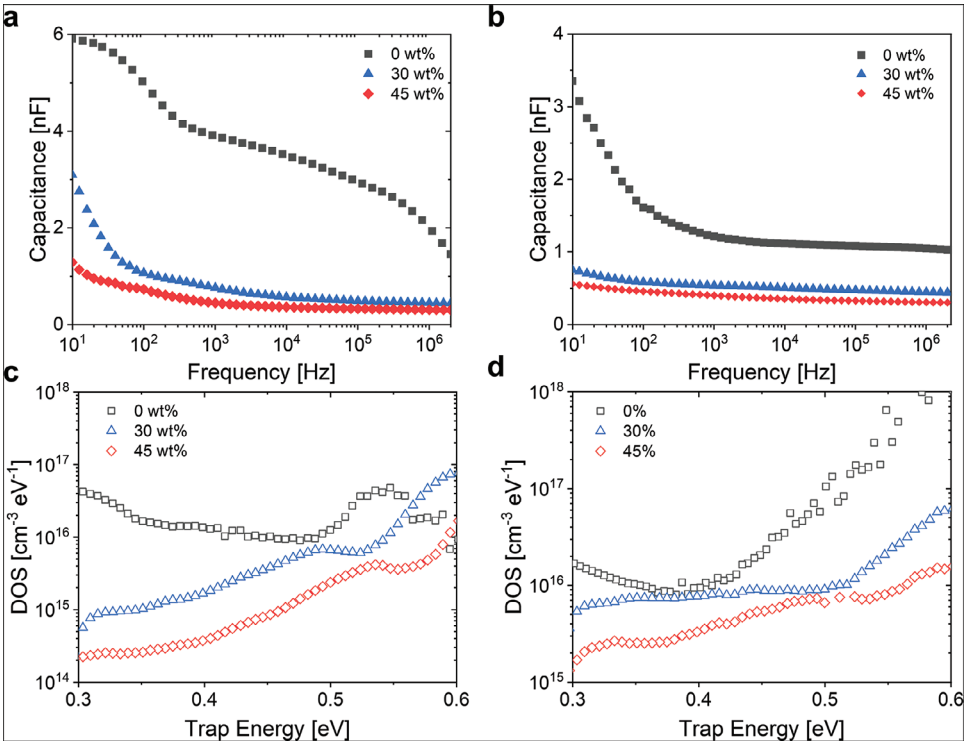

Figure 6. a) Capacitance–frequency measurements of the control device and 30 and 45 wt% PSU ternary blend devices at 0 V and b) at −2 V bias. c) Extracted density of states using a single Gaussian fitting at 0 V and d) under an applied bias of −2 V . Low frequency features are attributed to trap states within the bandgap.

to AC modulation and is expressed as a function of the measurement frequency by

$$E_\omega = kT \ln\left(\frac{\omega_0}{\omega}\right) \tag{4}$$

where k is Boltzmann's constant, T is the temperature, and ω_0 is the rate pre-factor for thermal excitation from the trap ($\approx 10^{12}$ s^{-1} in typical OPDs). The trap DOS distribution connects the materials composition and electronic properties, specifically to estimate the energy and number of localized trap states. It is extracted from the C–ω measurement according to Equation (5)

$$DOS\ (E_\omega) = -\frac{V_{bi}}{qAtkT}\frac{dC(\omega)}{d\ln(\omega)} \tag{5}$$

where V_{bi} is the built-in potential, q is the elementary charge, A is the device active area, t is the film thickness, and $C(\omega)$ is the capacitance measured with an AC perturbation of angular frequency, ω.[40–42] Here, V_{bi} ranges from 0.17 to 0.21 V for the different PSU concentrations at a temperature of 300 K. It is important to note that the capacitance measurement accounts for the sum of electron and hole traps rather than each carrier type exclusively.

The lower carrier mobilities of organic devices limit the frequency window over which charges can migrate in response to the AC perturbation and contribute to the capacitive response.[43,44] The transition between the depletion capacitance and the geometric capacitance regimes can create a sudden change in slope that impedes C–ω analysis.[44] However, the lack of a characteristic steep drop in capacitance at high frequencies in **Figure 6a** suggests that the devices remain fully depleted despite the increase in active layer thickness from 180 to 460 nm. This is further supported by the similar high frequency behavior at 30% and 45% PSU content as a reverse bias of −2 V is applied (Figure 6b). The C–ω behavior in the dark at 0 V bias demonstrates a rapid change in slope ($dC/d\omega$) at lower frequencies, which reflects an increase of the trap DOS. As shown in Figure 6c, we observe that with increasing concentration of PSU, the density of deep traps (0.45 to 0.6 eV) shifts further into the bandgap. This corresponds to changing $dC/d\omega$ of the devices with the progressive addition of PSU in the frequency range from 10^2–10^3 Hz. In addition, we observe the reduction of traps in the high-frequency region as PSU concentration increases, though this effect could be enhanced by the lowered mobilities and thicker depletion layers. Both trends in high and low energy traps are also observed in the calculated density of states distributions under bias.

To further quantify the deep trap states, we expressed the DOS using a single Gaussian distribution:

$$DOS\ (E_\omega) = \frac{N_G}{\sigma\sqrt{2\pi}} \exp\left[-\frac{(E_\omega - E_{G0})^2}{2\sigma^2}\right] \tag{6}$$

where the fitting yielded the density of deep states N_G, the disorder spread σ, and the mean energy of the deep traps E_{G0}. The DOS for different PSU concentrations are depicted in Figure 6c, and the best-fit values (Figure S12, Supporting Information) are

listed in Table S1 (Supporting Information). Figure 6c demonstrates the defect DOS distributions derived from the *C*–ω analysis using Equation (5). Distinct DOS distributions located at ≈0.35 and 0.55 eV are observed using a low concentration of PSU. When fitted with Equation (6), N_G is reduced using PSU from 2.98×10^{15} cm^{-3} in the control device (i.e., 0 wt%) to 0.46×10^{15} cm^{-3} in the 45 wt% device. Additionally, we observe a shift in the DOS trap distribution to energies above 0.6 eV as we increase the concentration of PSU. We attribute this shift to a reduction in the shallow traps into the deep traps that can be caused by the intercalation of PSU in the BHJ structure. Similar reductions in trap density via dilution of the charge carrier components with a wide bandgap polymer were observed by Abbaszadeh et al.[34,45] The Gaussian DOS distribution characterizes the localized, deep trap states in the band gaps of these ternary blends. Carriers trapped in these deep states, whether photogenerated, injected from the electrodes, or thermally excited, are less likely to be collected, as the energy required for the charge to escape from the localized state becomes higher than the available thermal energy. Thus, increasing deep traps may be the cause of the reduced EQE, while the decrease of the shallow trap density correlates with the reduction in the dark current. This reduction is also consistent with the microscopy images of the highest concentration (45 wt%) PSU ternary blend films with large insulator domains that can inhibit the percolation pathway of charge carriers. However, the reduction of traps encountered per unit volume of the active layer far outpaces the decreased access of the donor–acceptor materials to the device electrodes, thus the dark current is decreased to a greater degree than the photocurrent.

An additional mechanism that can contribute to the dark current in organic photodiodes under reverse bias is trap mediated generation. Here, carriers are thermally excited to an intermediate trap state before being excited again into a band.[32,46] In this scenario, the Shockley–Read–Hall (SRH) generation rate under reverse bias is given by Equation (7).

$$G = \frac{\beta_{SRH} N_t n_i}{2\cosh\left(\frac{E_t - E_i}{k_B T}\right)} \tag{7}$$

Here, β_{SRH} is the rate of recombination, N_t is the trap state density, n_i is the intrinsic carrier concentration, E_i is the energy at the middle of the bandgap and E_t is the trap state energy. The trap-assisted generation rate is therefore maximized as N_t increases and as the energy of the traps approaches the midgap energy of the charge transfer state. In the case of the binary CDT-TQ:$PC_{71}BM$ OPD under a −2 V bias, this is ≈0.41 eV from the band edge (Figure 6d) with a significant reduction in the trap DOS around this value as the PSU content is increased to 45%. A reduction in dark current is also consistent with the observed shift in trap DOS to very deep levels.

Finally, we examined the response time of the ternary blend OPD incorporating 45 wt% PSU with the control device. Figure S15 (Supporting Information) shows the normalized photocurrent of the devices under a reverse bias of −2 V responding to a 940 nm LED light with an irradiation power density of 10.0 mW cm^{-2}. The response time was determined from the rise time (τ_r) and fall time (τ_f), which are the times required to increase the signal amplitude of the steady-state photocurrent from 10 to 90% and 90 to 10%, respectively. The control device exhibited τ_r = 26.7 µs and τ_f = 30.7 µs, while the 45 wt% PSU device displayed τ_r = 41.0 µs and τ_f = 118.1 µs. Comparing the transient lifetimes, the longer fall time is indicative of a longer trapping release time, consistent with deep electron traps which remain present based on the DOS.

3. Conclusion

In summary, incorporating insulating polymers materials with the active layers of IR OPDs suppresses noise under reverse bias and increases the specific detectivity (D^*). We observe a systematic change in the photocurrent and dark noise as the content of insulator is increased. The insulating polymers lower the trap state density and carrier mobility in the blends and result in thicker films. While this reduces the total photocurrent, the dark noise decreased to a far greater extent. Thus, insulator-modified devices based on narrow bandgap conjugated polymers exhibit increased D^* despite a decrease in EQE. This study demonstrates that the incorporation of insulating polymers can alleviate the persistent noise issues with narrow bandgap photodetectors and enable their practical operation.

Supporting Information

Supporting Information is available from the Wiley Online Library or from the author.

Acknowledgements

The work performed at The Georgia Institute of Technology was made possible by the National Science Foundation (NSF) award DMR-2323665 and the Air Force Office of Scientific Research (AFOSR) under support provided by the Organic Materials Chemistry Program (Grant FA9550-23-1-0654, Program Manager: Dr. Kenneth Caster).

Conflict of Interest

The authors declare no conflict of interest.

Data Availability Statement

The data that support the findings of this study are available in the supplementary material of this article.

Keywords

donor–acceptor conjugated polymers, infrared photodetectors, organic photodiodes, organic semiconductors, semiconducting polymers

Received: November 12, 2023
Revised: January 22, 2024
Published online: February 19, 2024

[1] F. P. García de Arquer, A. Armin, P. Meredith, E. H. Sargent, *Nat. Rev. Mater.* **2017**, *2*, 16100.
[2] L. Dou, Y. Liu, Z. Hong, G. Li, Y. Yang, *Chem. Rev.* **2015**, *115*, 12633.
[3] Z. Wu, Y. Zhai, H. Kim, J. D. Azoulay, T. N. Ng, *Acc. Chem. Res.* **2018**, *51*, 3144.
[4] N. Li, P. Mahalingavelar, J. H. Vella, D.-S. Leem, J. D. Azoulay, T. N. Ng, *Mater. Sci. Eng. R Rep.* **2021**, *146*, 100643.
[5] R. D. Jansen-van Vuuren, A. Armin, A. K. Pandey, P. L. Burn, P. Meredith, *Adv. Mater.* **2016**, *28*, 4766.
[6] D. Yang, D. Ma, *Adv. Opt. Mater.* **2019**, *7*, 1800522.
[7] N. Strobel, M. Seiberlich, R. Eckstein, U. Lemmer, G. Hernandez-Sosa, *Flex. Print. Electron.* **2019**, *4*, 043001.
[8] A. Rogalski, *Infrared and terahertz detectors*, CRC Press, Boca Raton **2019**.
[9] L. Ding, Z.-D. Yu, X.-Y. Wang, Z.-F. Yao, Y. Lu, C.-Y. Yang, J.-Y. Wang, J. Pei, *Chem. Rev.* **2023**, *123*, 7421.
[10] G. Simone, M. J. Dyson, S. C. J. Meskers, R. A. J. Janssen, G. H. Gelinck, *Adv. Funct. Mater.* **2020**, *30*, 1904205.
[11] D. Meng, R. Zheng, Y. Zhao, E. Zhang, L. Dou, Y. Yang, *Adv. Mater.* **2022**, *34*, 2107330.
[12] N. Li, X. Hu, X. Sui, Q. Chen, T. N. Ng, *ACS Appl. Electron. Mater.* **2023**, *5*, 21.
[13] D. Zhu, D. Ji, L. Li, W. Hu, *J. Mater. Chem. C* **2022**, *10*, 13312.
[14] C. Wang, X. Zhang, W. Hu, *Chem. Soc. Rev.* **2020**, *49*, 653.
[15] A. Pierre, I. Deckman, P. B. Lechêne, A. C. Arias, *Adv. Mater.* **2015**, *27*, 6411.
[16] C. Fuentes-Hernandez, W.-F. Chou, T. M. Khan, L. Diniz, J. Lukens, F. A. Larrain, V. A. Rodriguez-Toro, B. Kippelen, *Science* **2020**, *370*, 698.
[17] S. Gielen, C. Kaiser, F. Verstraeten, J. Kublitski, J. Benduhn, D. Spoltore, P. Verstappen, W. Maes, P. Meredith, A. Armin, K. Vandewal, *Adv. Mater.* **2020**, *32*, 2003818.
[18] Z. Wu, W. Yao, A. E. London, J. D. Azoulay, T. N. Ng, *Adv. Funct. Mater.* **2018**, *28*, 1800391.
[19] G. Simone, M. J. Dyson, C. H. L. Weijtens, S. C. J. Meskers, R. Coehoorn, R. A. J. Janssen, G. H. Gelinck, *Adv. Opt. Mater.* **2020**, *8*, 1901568.
[20] A. E. London, L. Huang, B. A. Zhang, M. B. Oviedo, J. Tropp, W. Yao, Z. Wu, B. M. Wong, T. N. Ng, J. D. Azoulay, *Polym. Chem.* **2017**, *8*, 2922.
[21] F. Verstraeten, S. Gielen, P. Verstappen, J. Kesters, E. Georgitzikis, J. Raymakers, D. Cheyns, P. Malinowski, M. Daenen, L. Lutsen, K. Vandewal, W. Maes, *J. Mater. Chem. C* **2018**, *6*, 11645.
[22] F. Verstraeten, S. Gielen, P. Verstappen, J. Raymakers, H. Penxten, L. Lutsen, K. Vandewal, W. Maes, *J. Mater. Chem. C* **2020**, *8*, 10098.
[23] J. Huang, J. Lee, J. Vollbrecht, V. V. Brus, A. L. Dixon, D. X. Cao, Z. Zhu, Z. Du, H. Wang, K. Cho, G. C. Bazan, T.-Q. Nguyen, *Adv. Mater.* **2020**, *32*, 1906027.
[24] X. Yu, H. Lin, Z. He, X. Du, Z. Chen, G. Yang, C. Zheng, S. Tao, *ACS Appl. Mater. Interfaces* **2023**, *15*, 16918.
[25] E. L. Dereniak, G. D. Boreman, *Infrared detectors and systems*, John Wiley & Sons, New York **1996**.
[26] T. A. M. Ferenczi, C. Müller, D. D. C. Bradley, P. Smith, J. Nelson, N. Stingelin, *Adv. Mater.* **2011**, *23*, 4093.
[27] A. D. Scaccabarozzi, N. Stingelin, *J. Mater. Chem. A* **2014**, *2*, 10818.
[28] M. Wang, S. Liu, P. You, N. Wang, G. Tang, Q. Miao, F. Yan, *Sol. RRL* **2020**, *4*, 2000013.
[29] N. Strobel, R. Eckstein, J. Lehr, U. Lemmer, G. Hernandez-Sosa, *Adv. Electron. Mater.* **2018**, *4*, 1700345.
[30] U. Shafique, C. Santato, K. S. Karim, *IEEE Trans. Electron Devices* **2014**, *61*, 3465.
[31] W. Yao, Z. Wu, E. Huang, L. Huang, A. E. London, Z. Liu, J. D. Azoulay, T. N. Ng, *ACS Appl. Electron. Mater.* **2019**, *1*, 660.
[32] J. Kublitski, A. Hofacker, B. K. Boroujeni, J. Benduhn, V. C. Nikolis, C. Kaiser, D. Spoltore, H. Kleemann, A. Fischer, F. Ellinger, K. Vandewal, K. Leo, *Nat. Commun.* **2021**, *12*, 551.
[33] E. Go, H. Jin, S. Yoon, S. Park, S. H. Park, H. Yu, H. J. Son, *ACS Photonics* **2022**, *9*, 2056.
[34] D. Abbaszadeh, A. Kunz, G. A. H. Wetzelaer, J. J. Michels, N. I. Crăciun, K. Koynov, I. Lieberwirth, P. W. M. Blom, *Nat. Mater.* **2016**, *15*, 628.
[35] C. Wang, X. Liu, Y. Xiao, J. Bergqvist, X. Lu, F. Gao, M. Fahlman, *Sol. RRL* **2020**, *4*, 2000261.
[36] Z. Zhang, R. Shi, A. Amini, S. K. So, C. Cheng, *Phys. Status Solidi Rapid Res. Lett.* **2022**, *16*, 2100602.
[37] S. Riera-Galindo, F. Leonardi, R. Pfattner, M. Mas-Torrent, *Adv. Mater. Technol.* **2019**, *4*, 1900104.
[38] Z. Peng, N. Stingelin, H. Ade, J. J. Michels, *Nat. Rev. Mater.* **2023**, *8*, 439.
[39] H. F. Haneef, A. M. Zeidell, O. D. Jurchescu, *J. Mater. Chem. C* **2020**, *8*, 759.
[40] T. Walter, R. Herberholz, C. Müller, H. W. Schock, *J. Appl. Phys.* **1996**, *80*, 4411.
[41] P. P. Boix, G. Garcia-Belmonte, U. Muñecas, M. Neophytou, C. Waldauf, R. Pacios, *Appl. Phys. Lett.* **2009**, *95*, 233302.
[42] R. A. Street, Y. Yang, B. C. Thompson, I. McCulloch, *J. Phys. Chem. C* **2016**, *120*, 22169.
[43] S. Wang, P. Kaienburg, B. Klingebiel, D. Schillings, T. Kirchartz, *J. Phys. Chem. C* **2018**, *122*, 9795.
[44] L. Xu, J. Wang, J. W. P. Hsu, *Phys. Rev.Appl.* **2016**, *6*, 064020.
[45] D. Abbaszadeh, A. Kunz, N. B. Kotadiya, A. Mondal, D. Andrienko, J. J. Michels, G.-J. A. H. Wetzelaer, P. W. M. Blom, *Chem. Mater.* **2019**, *31*, 6380.
[46] O. J. Sandberg, C. Kaiser, S. Zeiske, N. Zarrabi, S. Gielen, W. Maes, K. Vandewal, P. Meredith, A. Armin, *Nat. Photonics* **2023**, *17*, 368.